

Article

Calibration of the Modified Mohr–Coulomb Failure Criterion and Its Application in the Study of Collision Response of Ship Hull Plate Frame Structures

Shiye Liu ¹, Kun Liu ^{1,*}, Hwei Liu ², Shuai Zong ¹, Yue Lu ¹ and Chuhao Liu ¹

¹ School of Naval Architecture and Ocean Engineering, Jiangsu University of Science and Technology, Zhenjiang 212003, China; l917715625@gmail.com (S.L.); 220110101103@stu.just.cn (S.Z.); yuelu@just.edu.cn (Y.L.); sunflee728@gmail.com (C.L.)

² School of Naval Architecture and Ocean Engineering, Huazhong University of Science and Technology, Wuhan 430074, China; wssls1w1@hust.edu.cn

* Correspondence: kunliu@just.edu.cn; Tel.: +86-135-1169-2085; Fax: +86-0511-8444-6543

Abstract: Within the lifecycle of a ship's hull structure, damage due to collisions has been a focal point of research for researchers both domestically and internationally. To enhance the predictive accuracy of failure criteria in the simulation of ship hull collisions, this paper focuses on the modified Mohr–Coulomb (MMC) failure criterion for metals, utilizing a hybrid experimental–numerical method for parameter calibration. Consideration of stress-state-dependent mesh size sensitivity has been amended, and the approach is integrated into the comprehensive nonlinear finite element software Abaqus 2020. Finite element tensile simulations were conducted to validate the effectiveness of the MMC criterion. Simulation analyses were conducted based on drop hammer collision experiments with various failure criteria and grid sizes. The comparative validation highlighted the superiority of the mesh size sensitivity-corrected MMC failure criterion. The outcomes of this research provide a foundation for assessing the structural safety of ship hulls.

Keywords: ship collision; MMC failure criterion; numerical simulation



Citation: Liu, S.; Liu, K.; Liu, H.; Zong, S.; Lu, Y.; Liu, C. Calibration of the Modified Mohr–Coulomb Failure Criterion and Its Application in the Study of Collision Response of Ship Hull Plate Frame Structures. *J. Mar. Sci. Eng.* **2024**, *12*, 805. <https://doi.org/10.3390/jmse12050805>

Academic Editor: Vincenzo Crupi

Received: 5 April 2024

Revised: 4 May 2024

Accepted: 4 May 2024

Published: 12 May 2024



Copyright: © 2024 by the authors. Licensee MDPI, Basel, Switzerland. This article is an open access article distributed under the terms and conditions of the Creative Commons Attribution (CC BY) license (<https://creativecommons.org/licenses/by/4.0/>).

1. Introduction

As computational power rapidly advances and finite element analysis (FEA) software continues to evolve, finite element methods have become an integral tool in the field of ship collision studies. Ships, being thin-walled structures, are generally modeled using shell elements in FEA, and failure of ship structures is often represented by the deletion of failed shell elements [1,2]. Thus, accurate prediction of the hull structural failure mode presupposes the definition of an appropriate failure criterion within the simulation software, which has traditionally been a major challenge in ship collision simulations.

Researchers at home and abroad have conducted extensive research on collision damage to ship metal structures. Minorsky [3] categorized the research on ship issues into two aspects: the internal mechanisms and the external mechanisms. The external mechanisms consider the ship as a rigid body, focusing on the six degrees of freedom of rigid motion, external loads applied to the ship, and the dissipation of kinetic energy. The internal mechanisms, on the other hand, are primarily concerned with the dynamic response of the ship's structure and its damage and deformation during a collision. Haris and Amdahl [4] proposed a procedure utilizing a simplified analysis method for examining ship collisions that takes into account the interaction between the impact deformation and the struck ship. Törnqvist [5] conducted research on the design of collision-resistant structures for ships in which the Rice–Tracey and Cockcroft–Latham (RTCL) failure criterion is calibrated and integrated into the LS-DYNA R12 simulation environment. Ehlers et al. [6] determined the impact of various failure criteria, such as mesh size sensitivity, on the

collision results by simulating the collision response of three distinct ship side structures using the finite element method. Storheim et al. [7] investigated the robustness of the fracture criterion, i.e., the ability to simulate fracture under different stress states and mesh sizes.

Concerning metal failure criteria, researchers have conducted numerous studies. Driemeier et al. [8] found that the introduction of notches in tensile specimens can effectively increase the stress triaxiality at the fracture location, leading to earlier failure of the specimen. Wang Zeping [9] integrated the Johnson–Cook (JC) and Gurson–Tvergaard–Needleman (GTN) models to develop an enhanced material model that addresses the GTN model’s accuracy limitations at high strain rates. In an exhaustive review of failure criteria employed in finite element analyses of ship collision events, M.A.G. Calle [10] identified the equivalent plastic strain failure criterion as notably suitable due to its high practicality and straightforward integration into prevalent finite element software.

Recent studies demonstrate that metal fracture strain is not only related to stress triaxiality but also to the Lode angle parameter. Bai and Wierzbicki [11], by modifying the Mohr–Coulomb criterion to predict the ductile fracture of metallic materials, proposed the modified Mohr–Coulomb (MMC). Lou et al. [12] and Hu et al. [13] scrutinized the precision and suitability of the ductile fracture criterion across varying stress triaxiality ranges using AA2024-T351 experimental data as compiled by Bao and Wierzbicki [14]. Their findings disclosed that conventional failure criteria, confined to stress triaxiality considerations, falter in accurately forecasting experimental outcomes across an extended triaxiality spectrum. In contrast, failure criteria that incorporate both stress triaxiality and the Lode angle parameter have demonstrated superior predictive capabilities across a comprehensive array of experimental conditions.

Compared to other failure criteria, the MMC failure criterion takes into account the effects of both stress triaxiality and the Lode angle on failure, and is able to forecast metal failure across a wider range of stress triaxialities and effectively simulate collision damage to metal structures under complex stress conditions. Therefore, it is essential to undertake the calibration of the MMC failure criterion and the mesh-size-based calibration and apply these to the collision response analysis of the ship’s hull panel–frame structure.

The MMC fracture criterion was used by Talebi-Ghadikolaee et al. [15] to examine the fracture behavior of an AA6061-T6 aluminum alloy sheet during U-shaped bending, while Voormeeren et al. [16] talked about how to apply the MMC failure criterion based on a single tensile test. The results of Zhu et al. [17]’s fine mesh simulation demonstrate that the shear force predicted by the MMC failure criterion is essentially in agreement with the data from the experiments.

In this study, to enable a more precise simulation of ship collision problems, a calibration was performed on the MMC failure criterion that accounts for stress triaxiality. The criterion was embedded into the large-scale nonlinear finite element software Abaqus via secondary development. Additionally, drop hammer tests on the hull panel–frame structure using the MMC failure criterion were conducted, along with corresponding simulations to investigate the deformation and damage mechanisms. By discussing the impacts of different failure criteria and mesh sizes on the simulation results, the validation of the MMC failure criterion’s superiority was confirmed following the adjustment for mesh sensitivity. This provides a basis for the safety assessment of hull girder structures.

2. MMC Failure Criterion

The Mohr–Coulomb criterion [18] is a type of stress-based failure criterion that is commonly used to evaluate failure in materials like rock, soil bodies, concrete, etc., that either fail in the elastic stage or only undergo slight plastic deformations. The Mohr–Coulomb criterion is expressed as follows in Equation (1):

$$\max(\tau + c_1\sigma_n)_f = c_2 \quad (1)$$

Here, τ and σ_n represent the shear stress and principal stresses on the fracture plane, respectively. c_2 is the shear strength and c_1 is the friction coefficient, which describes the relative weighting between the shear stress and normal stress. When $c_1 = 0$, the Mohr–Coulomb criterion degenerates into the maximum shear stress criterion. Therefore, the Mohr–Coulomb criterion can be viewed as an extension of the maximum shear stress criterion, as it can simultaneously describe fracture behavior caused by both normal and shear stresses.

Since any stress inside a material can be represented in the Cartesian coordinate system $(\sigma_1, \sigma_2, \sigma_3)$ formed by the three principal stresses, any stress can also be expressed in the cylindrical coordinate system $(\bar{\sigma}, \eta, \bar{\theta})$ formed by the equivalent stress, stress triaxiality, and Lode angle parameters. Bao and Wierzbicki [19] extended the application range of the Mohr–Coulomb criterion by transforming Equation (1) into a function of $(\bar{\sigma}, \eta, \bar{\theta})$ and proposed the MMC failure criterion for predicting ductile fracture in metallic materials. Its original expression is shown in Equation (2):

$$\bar{\epsilon}_f = \left\{ \frac{K}{c_2} [1 - c_\eta(\eta - \eta_0)] \times \left[c_\theta^s + \frac{\sqrt{3}}{2-\sqrt{3}} (c_\theta^{ax} - c_\theta^s) \left(\sec\left(\frac{\bar{\theta}\pi}{6}\right) - 1 \right) \right] \right\}^{-\frac{1}{n}} \times \left[\frac{\sqrt{1+c_1^2}}{3} \cos\left(\frac{\bar{\theta}\pi}{6}\right) + c_1 \left(\eta + \frac{1}{3} \sin\left(\frac{\bar{\theta}\pi}{6}\right) \right) \right] \tag{2}$$

$$c_\theta^{ax} = \begin{cases} 1, & \bar{\theta} \geq 0 \\ c_\theta^c, & \bar{\theta} < 0 \end{cases} \tag{3}$$

where K and n are the hardening coefficients and hardening exponents, respectively, in the hardening criteria, which can be obtained by fitting the true stress–strain curve from uniaxial tension tests. c_1 and c_2 are material parameters in the original Mohr–Coulomb criterion, which can be calibrated through a combination of experimental tests and numerical simulations using optimization algorithms to determine the parameters of the three-dimensional fracture surface, c_1 and c_2 . Parameter c_θ^c, c_θ^s is associated with the asymmetry of the fracture surface. When the material follows the von Mises yield criterion (i.e., isotropic hardening), $c_\eta = 0$ and $c_\theta^s = c_\theta^c = 1$, Equations (2) and (3) can be simplified as follows:

$$\bar{\epsilon}_f = \left\{ \frac{K}{c_2} \left[\frac{\sqrt{1+c_1^2}}{3} \cos\left(\frac{\bar{\theta}\pi}{6}\right) + c_1 \left(\eta + \frac{1}{3} \sin\left(\frac{\bar{\theta}\pi}{6}\right) \right) \right] \right\}^{-\frac{1}{n}} \tag{4}$$

In the plane stress state, there is a one-to-one correspondence between the Lode angle parameter and stress triaxiality, as shown in Equation (5). By substituting Equation (5) into Equation (4), which represents the fracture surface of the MMC failure criterion in $(\bar{\theta}, \eta, \bar{\epsilon}_f)$ three-dimensional (3D) space, the fracture failure trajectory in $(\eta, \bar{\epsilon}_f)$ two-dimensional (2D) space can be obtained and is displayed in Figure 1.

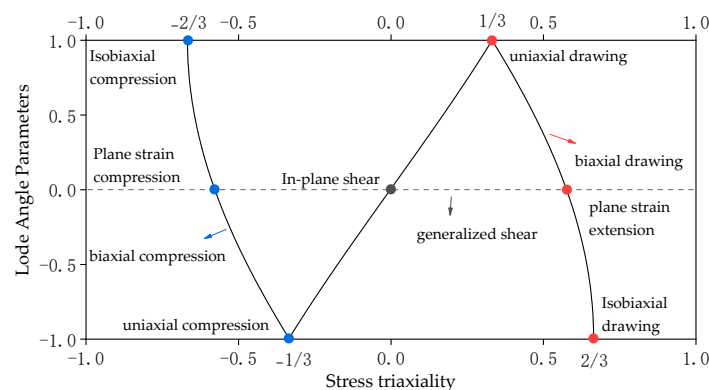


Figure 1. Stress states in the dimension of $(\eta, \bar{\theta})$.

$$\bar{\theta} = -\frac{2}{\pi} \arcsin \left[\frac{27}{2} \eta \left(\eta^2 - \frac{1}{3} \right) \right] \tag{5}$$

2.1. MMC Failure Criterion Parameter Fitting

In the parameter calibration process of the MMC failure criterion, Bai and Wierzbicki [11] adopted the basic procedure proposed for determining the failure criterion parameters in the $(\eta, \bar{\epsilon}_f)$ two-dimensional space, and further applied it to the calibration of parameters for the three-dimensional fracture surface in the $(\eta, \bar{\epsilon}_f, \bar{\theta})$ space. The specific steps are as follows:

Firstly, material testing is performed on specimens under different stress states to obtain their load–displacement curves. According to the setup of the experimental conditions, corresponding finite element simulation simulations are carried out. Critical data, such as the equivalent strain, stress triaxiality, and Lode angle parameters, are extracted from the finite element model, and their evolution curves are plotted with respect to the equivalent strain changes over the course of stress triaxiality and Lode angle parameters. Based on these curves, the average stress triaxiality and average Lode angle or average Lode angle parameters (where this study’s MMC fitting selects the average Lode angle parameter) are calculated using Equation (6). The fracture strain, average stress triaxiality, and average Lode angle parameters obtained from these calculations are then used to calibrate the undetermined parameters within the fracture criterion.

$$\begin{cases} \bar{\eta} = \frac{1}{\bar{\epsilon}_f} \int_0^{\bar{\epsilon}_f} \eta(\bar{\epsilon}) d\bar{\epsilon} \\ \bar{L} = \frac{1}{\bar{\epsilon}_f} \int_0^{\bar{\epsilon}_f} L(\bar{\epsilon}) d\bar{\epsilon} \\ \bar{\theta} = \frac{1}{\bar{\epsilon}_f} \int_0^{\bar{\epsilon}_f} \bar{\theta}(\bar{\epsilon}) d\bar{\epsilon} \end{cases} \tag{6}$$

Yu [20] conducted experimental and simulation studies on the plastic and fracture characteristics of marine high-strength steel under different stress states. Their tensile tests primarily included tensile and shear stress states. The literature provides the average stress triaxiality and average Lode angle parameters of the critical element at the failure location of different specimens, along with the corresponding failure strain (see Table 1). This paper, based on the data from the literature, employs MATLAB 2018b optimization tools to fit the MMC failure criterion.

Table 1. Fracture strain under different stress triaxiality and Lode angle.

Sample Type	Specimen Number	Stress Triaxiality η	Lode Angle $\bar{\theta}$	Failure Strain $\bar{\epsilon}_f$
Notched round bar	NRB6	0.443	1	1.091
	NRB1.5	0.716	1	0.910
Grooved plate	FGP12	0.593	0	0.905
	FGP1.8	0.765	0	0.830
Notched plate	NP20	0.446	0.614	1.018
	NP6.67	0.554	0.213	0.973
Shear	SH	−0.037	0.024	0.859

Generally speaking, the structural steel of a ship’s hull can be considered an isotropic material. The MMC failure criterion can be simplified from Equations (2)–(4) based on the von Mises criterion’s premises, where K and n reference the parameters of the Swift model in the literature [20], which are $K = 909.29$ MPa, $n = 0.1992$. Equation (7) is obtained.

$$\bar{\epsilon}_f = \left\{ \frac{909.29}{c_2} \left[\frac{\sqrt{1+c_1^2}}{3} \cos\left(\frac{\bar{\theta}\pi}{6}\right) + c_1 \left(\eta + \frac{1}{3} \sin\left(\frac{\bar{\theta}\pi}{6}\right) \right) \right] \right\}^{-\frac{1}{0.1992}} \tag{7}$$

At this point, the MMC failure criterion only involves two undetermined parameters, c_1 and c_2 . Utilizing the data from Table 1 and the optimization tool lsqcurvefit in MATLAB, the parameters c_1 and c_2 in Equation (7) are optimized to obtain the best-fitting 3D fracture surface. The lsqcurvefit function in MATLAB requires an initial set of solutions c_1 and c_2 . By substituting the data from specimens 4 and 5 into the aforementioned equation, initial values of $c_1 = -0.0207$ and $c_2 = 278.23$ MPa can be determined. Taking these values as the initial solutions and applying the least squares error optimization, the final MMC failure criterion parameters can be acquired. The MMC failure criterion parameters are then listed in Table 2.

Table 2. Parameters in the MMC failure criterion.

K	N	c_1	c_2
909.29 MPa	0.1992	0.0420	301.47 MPa

The final derived MMC failure criterion is presented as Equation (8):

$$\bar{\epsilon}_f = \left\{ \frac{909.29}{301.47} \left[\frac{\sqrt{1+0.042^2}}{3} \cos\left(\frac{\bar{\theta}\pi}{6}\right) + 0.042 \left(\eta + \frac{1}{3} \sin\left(\frac{\bar{\theta}\pi}{6}\right) \right) \right] \right\}^{-\frac{1}{0.1992}} \tag{8}$$

Using the cftool utility in MATLAB, the aforementioned equation is plotted in the $(\eta, \bar{\theta}, \bar{\epsilon}_f)$ space as shown in Figure 2, where the red line represents the fracture trajectory under the plane stress state.

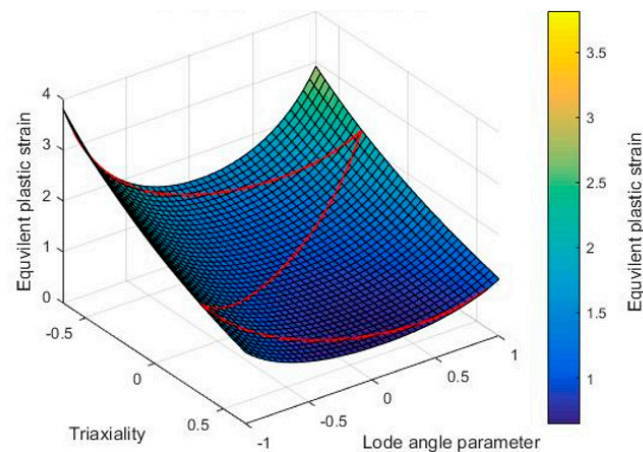


Figure 2. The MMC failure fracture surface of marine high-strength steel.

In ship collision simulation computations, where the finite element type employed is a plane stress shell element, the relationship between the stress triaxiality and the Lode angle parameter under plane stress conditions, as described in Equation (5), is substituted into Equation (8). This yields the fracture trajectory for the MMC failure criterion under plane stress conditions. The curve within the $(\eta, \bar{\epsilon}_f)$ space is depicted in Figure 3.

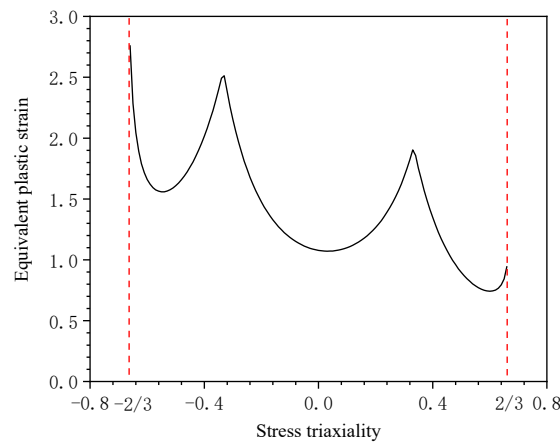


Figure 3. MMC failure locus in $(\eta, \bar{\epsilon}_f)$ dimension.

It should be noted that the parameters for the MMC failure criterion obtained here are based on solid elements with a size of 0.1 mm acquired through experimental–simulation hybrid analysis. These parameters are not directly applicable to ship collision simulations that employ shell elements. Consequently, a modification is necessary to adapt them for use in the simulation analysis of ship structural collisions.

2.2. Mesh Size Sensitivity Correction of the MMC Failure Criterion

The MMC failure criterion is established based on solid elements [11]. When this criterion is applied to shell elements, which operate under the assumption of plane stress and thus neglect variations in stress across the thickness, it results in a heightened sensitivity to the size of the shell element mesh. As the grid size of the shell elements is substantially greater than the plate thickness, in conducting finite element failure simulations with ductile metal plate materials using shell elements, scaling of the failure strain becomes necessary when the dimensions of the shell elements surpass the necking length. This scaling ensures that the necking phenomenon can be evenly distributed along the length of the element, thus enabling a precise determination of structural failure. Due to the necking, the failure strain of shell elements is significantly affected by the size of the element. Consequently, for shell elements with disparate grid sizes, it is imperative to adjust the failure strain accordingly to maintain the fidelity of the simulation.

Adjustments to failure criteria are commonly grounded on the results of uniaxial tension tests. For instance, the critical equivalent plastic strain criterion as well as the RTCL failure criterion can be scaled using the relation presented in Equation (9):

$$\bar{\epsilon}_f = n + (\epsilon_n - n) \frac{t}{l} \tag{9}$$

Herein, ϵ_n represents the input value for fracture strain at the occurrence of $t/l = 1$, while n is the strain hardening exponent, indicative of the strain at the onset of necking during uniaxial tension. The grid size sensitivity of the failure strain is attributed to the necking phenomenon; given that the degree of necking varies under different stress states, it can be surmised that any adjustments for grid size sensitivity of the failure strain should also take into account the influence of the stress state (stress triaxiality).

This article adopts a correction method that considers both grid size sensitivity and stress state. The crux lies in altering the fracture strain ϵ_n , in Equation (9), and the diffuse necking condition n to become functions of the stress triaxiality η . Utilizing $\bar{\epsilon}_{f,cal}(\eta)$ to substitute ϵ_n in Equation (9), the following formula can be obtained:

$$\epsilon^*(\eta) = \bar{\epsilon}_N(\eta) + \left(\bar{\epsilon}_{f,cal}(\eta) - \bar{\epsilon}_N(\eta) \right) \frac{L_{cal}}{t_{cal}} \tag{10}$$

In this context, L_{cal} and t_{cal} represent the characteristic element size and the plate thickness, respectively, used when calibrating the failure criterion parameters. For the MMC failure criterion discussed in this paper, a solid element size of 0.1 mm is adopted for calibration, and the plate specimen thickness used for parameter calibration is 2 mm. Thus, it follows that $L_{cal} = 0.1$ mm and $t_{cal} = 2$ mm. By incorporating the stress-triaxiality-dependent failure fracture trajectory, denoted by $\bar{\epsilon}_{f,cal}(\eta)$, and the Swift local necking curve, denoted by $\bar{\epsilon}_N(\eta)$, into Equation (10), one can obtain the failure trajectory $\epsilon^*(\eta)$ for $t/L = 1$ shell elements, as depicted in Figure 4.

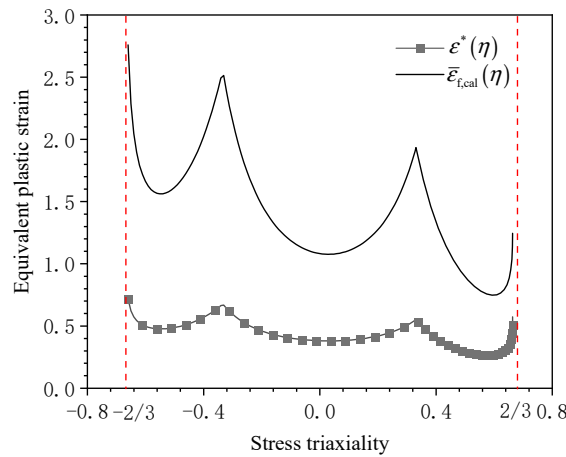


Figure 4. Calculate $\epsilon^*(\eta)$ according to $\bar{\epsilon}_{f,cal}(\eta)$.

Subsequently, through the inversion of Equation (10), the failure strain function that corresponds to any characteristic element length, denoted as $\bar{\epsilon}_f(L, t, \eta)$, can be derived, as demonstrated in Equation (11). With Equation (11), a series of the MMC failure criterion curves associated with different t/L values can be obtained through interpolation, as illustrated in Figure 5.

$$\bar{\epsilon}_f(L, t, \eta) = \bar{\epsilon}_N(\eta) + (\epsilon^*(\eta) - \bar{\epsilon}_N(\eta)) \frac{t}{L} \tag{11}$$

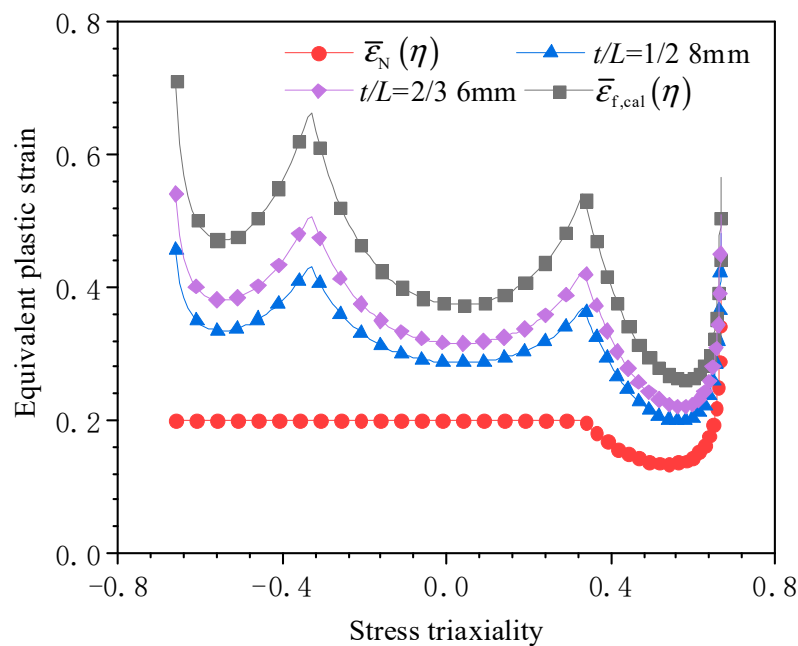


Figure 5. The MMC failure loci with different mesh sizes in $(\eta, \bar{\epsilon}_f)$ dimension.

It should be mentioned that the Swift necking curve typically exists in the (ϵ_1, ϵ_2) space. The expression of the load stress ratio, represented by the symbol $\alpha = \sigma_2/\sigma_1$, can be described as follows, assuming that it stays constant:

$$\begin{cases} \epsilon_1 = \frac{2(2-\alpha)(1-\alpha+\alpha^2)}{4-3\alpha-3\alpha^2+4\alpha}n \\ \epsilon_2 = \frac{2(2\alpha-1)(1-\alpha+\alpha^2)}{4-3\alpha-3\alpha^2+4\alpha}n \end{cases} \quad (12)$$

In order to convert Equation (12), which exists within the (ϵ_1, ϵ_2) space, to the curve $\bar{\epsilon}_N(\eta)$ within the $(\eta, \bar{\epsilon}_f)$ space as reflected in Equation (10) to Equation (11), the following transformations, represented by Equations (13)–(15), need to be applied to Equation (12).

Under the condition of plane stress, the equivalent plastic strain can be expressed as follows:

$$\bar{\epsilon} = \frac{2}{\sqrt{3}}\sqrt{1 + \beta + \beta^2} \cdot \epsilon_1 \quad (13)$$

In the equation, β represents the strain ratio, defined by $\beta = \epsilon_2/\epsilon_1$. Based on the von Mises criterion, there is a one-to-one correspondence between stress and strain under plane stress conditions. Consequently, the strain ratio β is related to the stress ratio α as follows:

$$\alpha = \frac{2\beta + 1}{\beta + 2} \quad (14)$$

Therefore, the stress triaxiality can also be obtained by calculating through the strain ratio.

$$\eta = \frac{1}{\sqrt{3}} \frac{1 + \beta}{\sqrt{1 + \beta + \beta^2}} = \frac{1 + \alpha}{\sqrt{1 - \alpha + \alpha^2}} \quad (15)$$

Based on Equations (13)–(15), the Swift instability curve in the (ϵ_1, ϵ_2) space can be transformed into a curve $\bar{\epsilon}_N(\eta)$ in the $(\eta, \bar{\epsilon}_f)$ space. Since the Swift curve corresponds to a stress range between uniaxial tension and equi-biaxial tension ($1/3 \leq \eta \leq 2/3$), to facilitate scaling the MMC failure criterion throughout the entire range of plane stress states, $\bar{\epsilon}_N(\eta) = n$ is selected within the $(-2/3 \leq \eta \leq 1/3)$ range, resulting in Equation (16). This is plotted in the $(\eta, \bar{\epsilon}_f)$ space as shown in Figure 5.

$$\bar{\epsilon}_N(\eta) = \begin{cases} n & -2/3 \leq \eta < 1/3 \\ \text{Swift necking curve} & 1/3 \leq \eta \leq 2/3 \end{cases} \quad (16)$$

2.3. The MMC Failure Criterion Embedding and Verification

2.3.1. Development of a VUMAT Subroutine

Abaqus, as a well-established general-purpose finite element software, offers 42 user subroutine interfaces that allow users to customize material properties, boundary conditions, special elements, and complex loads, as well as interfaces with other programs. The material subroutines UMAT and VUMAT enable users to implement their own algorithms and constitutive models of materials. In the domain of ship collision, the focus is often on the deformation process and residual deformation of structures under external loads. Thus, the implementation of the MMC failure criterion within finite element analysis is achieved using the VUMAT subroutine [21].

2.3.2. Simulation of Standard Test Specimens

To confirm the updated MMC failure criterion, quasi-static uniaxial tensile tests are designed and executed utilizing marine-grade high-strength steel, per the rules found in Metallic materials—Tensile testing at high strain rates—Part 1: Elastic-bar-type systems (GB/T 30069.1-2013). The tensile specimens and their dimensions are depicted in Figure 6. To ensure the reliability of the test results, three identical specimens are fabricated and three sets of material tensile tests are performed. To guarantee that the specimen is loaded under

quasi-static conditions, the test equipment’s tensile speed is controlled at 1.0 mm/min. The load experienced by the specimen and the elongation during the tensile process are recorded by the sensors integrated within the testing apparatus, enabling the acquisition of the load–displacement curve.

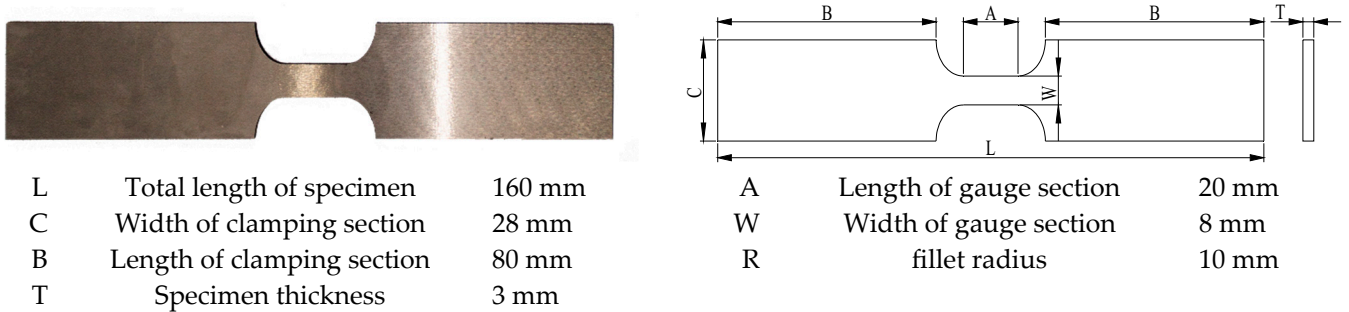


Figure 6. Quasi-static tensile test specimen size diagram.

The load–displacement curves obtained from the experimental results were converted into engineering stress–strain curves based on the effective cross-sectional dimensions of the actual specimens, as shown in Figure 7a. The conversion of the engineering stress–strain curves to true stress–strain was achieved by employing the composite relation curve of weighted averages proposed by Ling [22], as depicted in Figure 7b. The resulting parameters for the marine-grade high-strength steel are presented in Table 3.

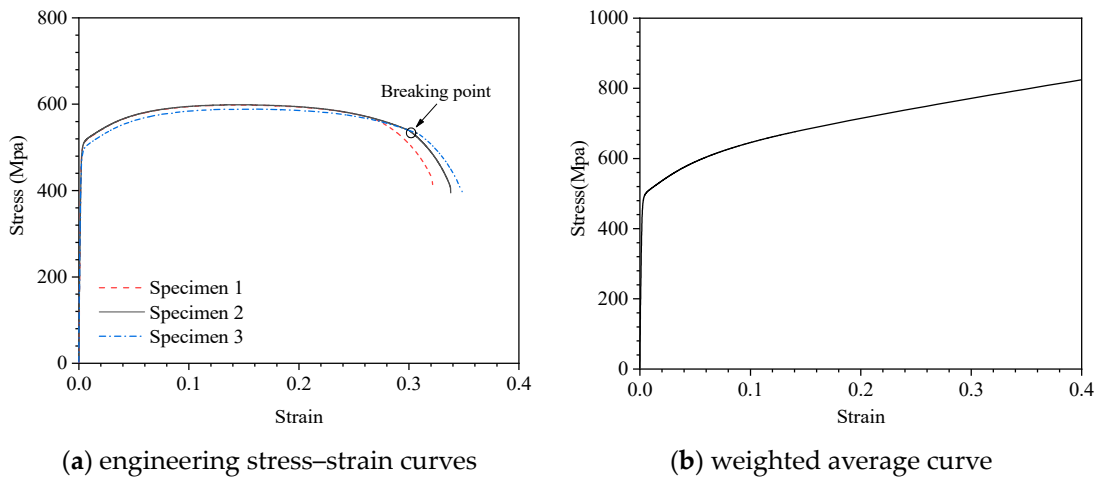


Figure 7. Stress–strain curve for marine-grade high-strength steel.

Table 3. Marine-grade high-strength steel material parameters.

Density ρ kg/m ³	Elastic Modulus E Gpa	Poisson Ratio	Yield Stress Mpa	Failure Strain
7850	210	0.3	470	0.28

For finite element simulation based on material testing, a finite element model is established for the middle parallel section of the specimen. Due to size limitations of the specimen, this part is discretized into finite element models of merely two mesh sizes, controlling the central element dimensions straining in the tensile direction to be 3 mm and 4 mm, respectively. The finite element model is illustrated in Figure 8. Reference points are established at the midpoints of both ends of the parallel section and are coupled to the respective ends; one reference point is rigidly constrained while the other point is allowed to release displacement in the tensile direction only. The displacement loading rate and mass scaling are maintained as consistent with the preceding section.

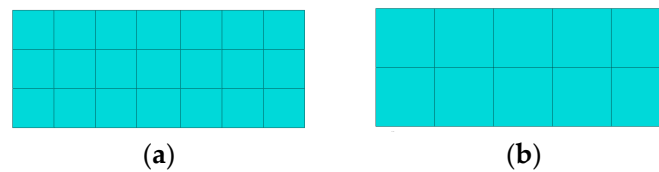


Figure 8. Finite element model of parallel section of standard specimen: (a) 3 mm × 2.7 mm; (b) 4 mm × 4 mm.

Due to the utilization of standard specimens, the engineering stress–strain curve can be deduced from the load–displacement graph. In Figure 9, a comparison of the engineering stress–strain curves for two different mesh sizes with the experimental data reveals a good agreement, which suggests that the MMC failure criterion can accurately predict the behavior of the standard tensile specimens addressed in this study.

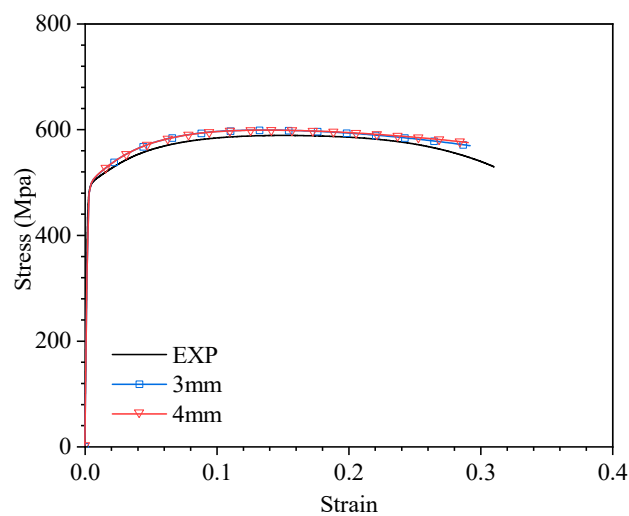


Figure 9. Comparison between experimental data and numerical force versus displacement curves.

3. Application of the MMC Failure Criterion in the Simulation of Ship Plate Frame Structure Collisions

3.1. Experimental Setup

The collision impact tests were conducted on the 50 kJ drop hammer impact testing apparatus at Jiangsu University of Science and Technology. This apparatus consists of counterweights, guide rails, an accelerometer, a hammer head, a buffer, displacement sensors, and supports. The main frame of the test apparatus is 6.3 m high, with a wedge-shaped hammer head width of 420 mm. The hammer head can be lifted to a maximum height of 3.7 m, achieving a maximum impact speed of 8.5 m/s. The maximum mass of the hammer head and counterweight system is 1350 kg, capable of generating a maximum impact energy of approximately 50 kJ. An accelerometer is affixed to the hammer body to calculate collision forces generated during the drop hammer test, while displacement sensors located on both sides of the support record the positional changes of the hammer body. The test apparatus and the wedge-shaped hammer head are depicted in Figure 10.

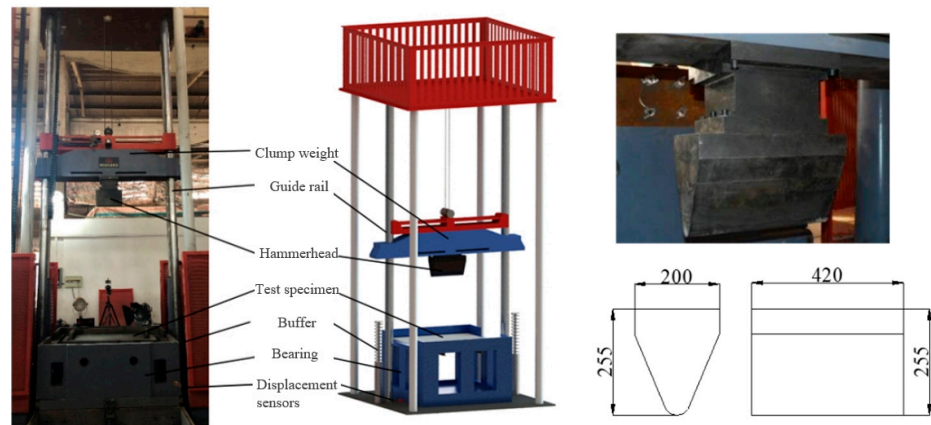


Figure 10. Fifty-kilojoule drop-weight impact test apparatus with a wedge-shaped hammer diagram (unit: mm).

3.2. Test Specimen Design

Based on the collision scenario depicted in Figure 11, which involves a little contact between the bow and the plate frame, we constructed the experiment. The plate frame specimens used in the experiments were fabricated from high-strength marine steel, with dimensions as shown in Table 4. A flange, 30 mm in width, was retained around the periphery of the specimen’s faceplate. The plate frame is inserted into the tooling through the panel’s reserved flange, and the tooling is welded to the plate frame, dimensionally corresponding to the actual object as depicted in Figure 12. The tooling is sufficiently rigid to be considered a rigid body and is attached to the foundation. Furthermore, it is important to minimize the heat effect of the plastic deformation of the structure during the welding process. Additionally, the tooling position needs to be adjusted to guarantee that the hammer head and the plate frame are centered. The high carbon chromium bearing steel (GCr15) impact hammer head is wedge-shaped and attached to the hammer body with a counterweight block to generate impact energy.

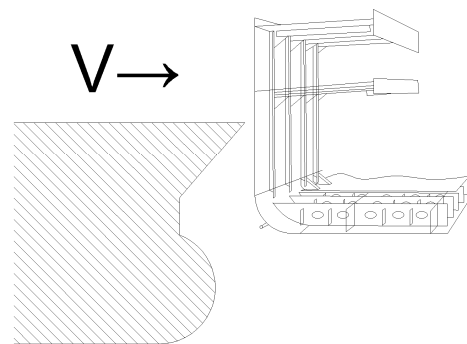


Figure 11. Diagrammatic representation of the crash site.

Table 4. The size of specimens (unit: mm).

Specimen Name	Quilting Material Spacing	Falling Weight Height	Slab Dimension	Bone Size	Bone Spacing	Truss Size
Plate frame structure	1000	2000	1560 × 1560 × 4	6# bulb flat	390	⊥ $\frac{4 \times 160}{5 \times 80}$

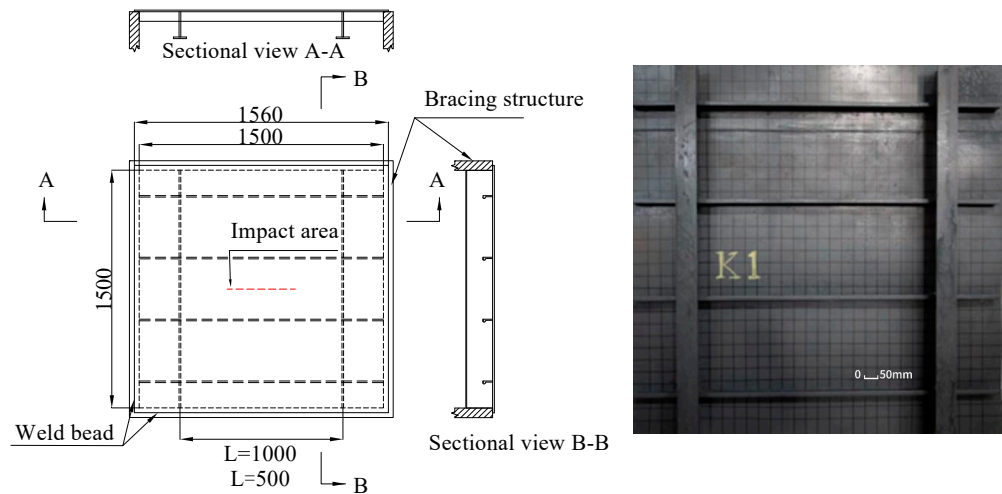


Figure 12. The dimension and picture of plate frame structure (Unit: mm).

3.3. Finite Element Model

Finite element models of the plate frame structure were constructed for drop hammer impact, as shown in Figure 13a. Models comprised both the plate frame structure and the impactor. Following the hammer head dimensions provided in Figure 14, a rigid hammer head was created in the finite element simulation with a mass of 1350 kg. The mesh size for the contact area between the hammer head and the panel was set to 4 mm, and the plate frame structures model is depicted in Figure 13b. In the finite element software, a reference point was added to the rigid hammer head, along with a mass of 1350 kg, and only the degrees of freedom in the Uz direction were released.

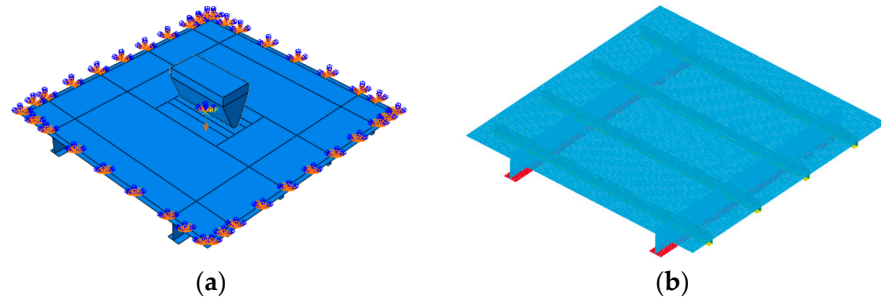


Figure 13. The finite element model of drop indenter impact scene. (a) Geometric model; (b) finite element model.

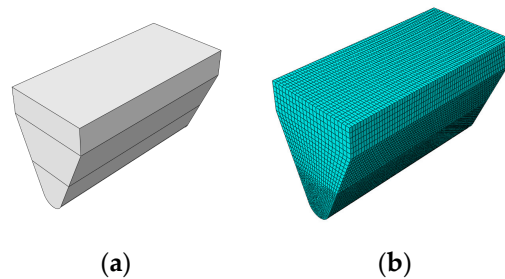


Figure 14. The geometry and finite element model of wedge indenter. (a) Geometric model; (b) finite element model.

In simulation calculations, the boundary conditions of the plate frame model should align as closely as possible with the actual experimental setup. The outer boundaries of the plate frame are welded to the support structure and can be considered as rigidly fixed. Therefore, the simulation involves applying fixed constraints to the external edges of the

plate frame ($U_x = U_y = U_z = UR_x = UR_y = UR_z = 0$) [23]. The inner boundaries of the plate frame are supported by the support structure; thus, the simulation restricts their displacement in the vertical direction ($U_z = 0$).

The material model for the metal plate frame is the same as described in Section 2.3.2, which is marine-grade high-strength steel. To account for the material’s strain rate effects, the Cowper–Symonds (C-S) model is employed to describe its strain rate effect. This model is characterized by its applicability within the medium to low strain rate range and is widely used in ship collision simulation calculations. The expression for the Cowper–Symonds model is as follows:

$$\frac{\sigma_d}{\sigma_s} = 1 + \left(\frac{\dot{\epsilon}}{D} \right)^{q-1} \tag{17}$$

The dynamic yield stress is denoted by σ_d , while σ_s represents the static yield stress, which can be obtained through uniaxial tensile tests. $\dot{\epsilon}$ denotes the equivalent plastic strain rate, and D and q are the Cowper–Symonds (C-S) constants, obtainable through fitting with dynamic testing data. For marine-grade high-strength steel, high-speed tensile tests at various strain rates were performed, resulting in material engineering stress–strain curves at different strain rates as shown in Figure 15. It can be observed that, with increasing strain rates, the flow stress of the marine structural steel continuously increases; furthermore, the toughness of this type of marine structural steel also increases with strain rate, a characteristic that significantly differs from low-carbon steels. The yield stresses from high-speed tensile tests at different strain rates were extracted as presented in Table 5. Fitting these data with the C-S constitutive model, values of $D = 678,000$ and $q = 5.261$ are obtained, as illustrated in Figure 16. The parameters for the marine-grade high-strength steel material are presented in Table 6.

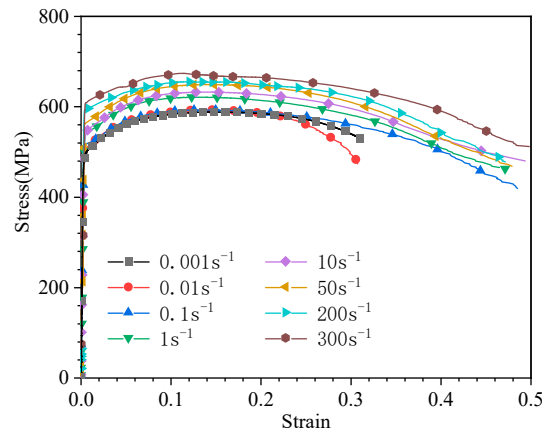


Figure 15. Strain–stress curves at different strain rates.

Table 5. Dynamic and static mechanical behavior of marine high-strength steel.

strain rate/s ⁻¹	0.001	0.01	0.1	1	10	50	200	300
yield stress/MPa	489	501	516	540	541	561	592	608

Table 6. Marine-grade high-strength steel material parameters.

Density ρ kg/m ³	Elastic Modulus E Gpa	Poisson Ratio	Yield Stress Mpa	Failure Strain	D	q
7850	210	0.3	470	0.28	678,000	5.261

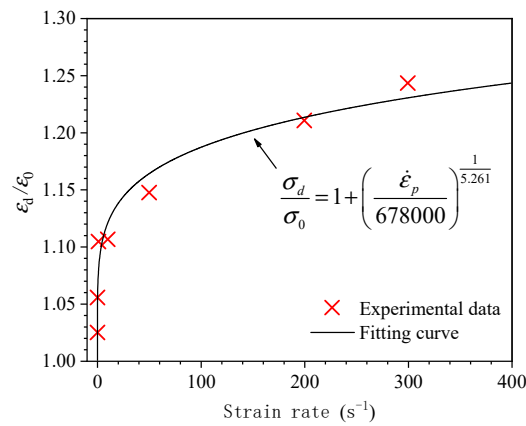


Figure 16. Cowper–Symonds model fitted by dynamic tensile data.

The contact type between the plate frame and hammer head is designated as “general contact”, with the contact properties’ normal behavior set as “hard contact” and tangential behavior chosen as “penalty”, with a friction coefficient of 0.3 as per reference [24].

3.4. Comparison of Simulation and Test Results

3.4.1. Damage Deformation

Figure 17 presents the results of the plate frame experiments under drop-weight impact loading compared to the damage contour maps computed using the MMC failure criterion. It is observable that panel indentation occurred around the impact area; due to the support provided by the stiffeners, the indented area was confined within the boundaries framed by the stringers and the web members, resulting in an elliptical indentation whose major axis aligns with the direction of the wedge-shaped head’s length. The deformation of the panels on either side of the impact mid-region was less significant, a phenomenon attributed to the initial shear failure at the panel edges beside the wedge-shaped impactor, which inhibited the efficient transmission of subsequent impact energies outward. The structure and load are symmetrical with respect to the longitudinal axis, but the response is not symmetrical, and this phenomenon occurs because the shape of the spherical flat steel in the plate frame is asymmetrical, so the resulting response is also asymmetrical.

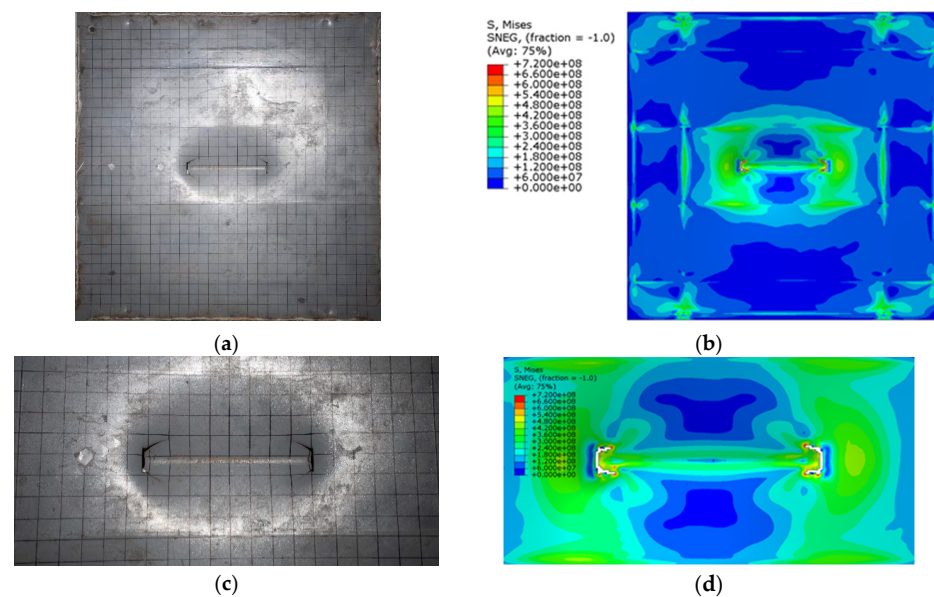


Figure 17. Contour of von Mises stress of plate frame under drop hammer collision condition. (a) Overall damage image; (b) overall contour of von Mises stress; (c) localized damage image; (d) localized contour of von Mises stress.

From the perspective of the damage state, the drop-weight impact loading tests revealed a “crescent-shaped” rupture in the plate frame structure, which showed good correspondence with the simulation results. Further analysis of the collision history contour maps, as indicated in Figure 18, reveals that the initial impact led to straight shear fracture, and the geometric continuity disruption at the fracture caused the load-bearing state of the structure at the rupture to evolve from a vertical shear to a coupled tearing of shear and in-plane tension. As a result, the fracture direction shifted from a parallel cut relative to the edge of the wedge head to a more obliquely oriented incision toward the direction of the wedge head’s length. With progressive deepening of the fracture, shear effects diminished while tensile effects increased, indicating a gradual inclination of the rupture direction toward the wedge head’s longitudinal direction.

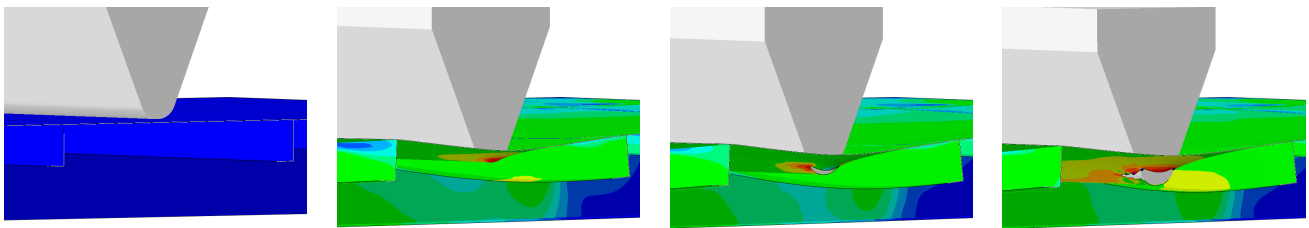


Figure 18. Damage deformation process of plate frame.

The measurement of plastic strain is conducted using the measure points indicated in Figure 19, and the overall deformation trend of the experiment and the three calculation methods is compared. It is evident that the trend of the MMC failure criterion is more similar to the experiment than the other two, and that the overall deformation trend of the three calculation methods is similar to the experimental results.

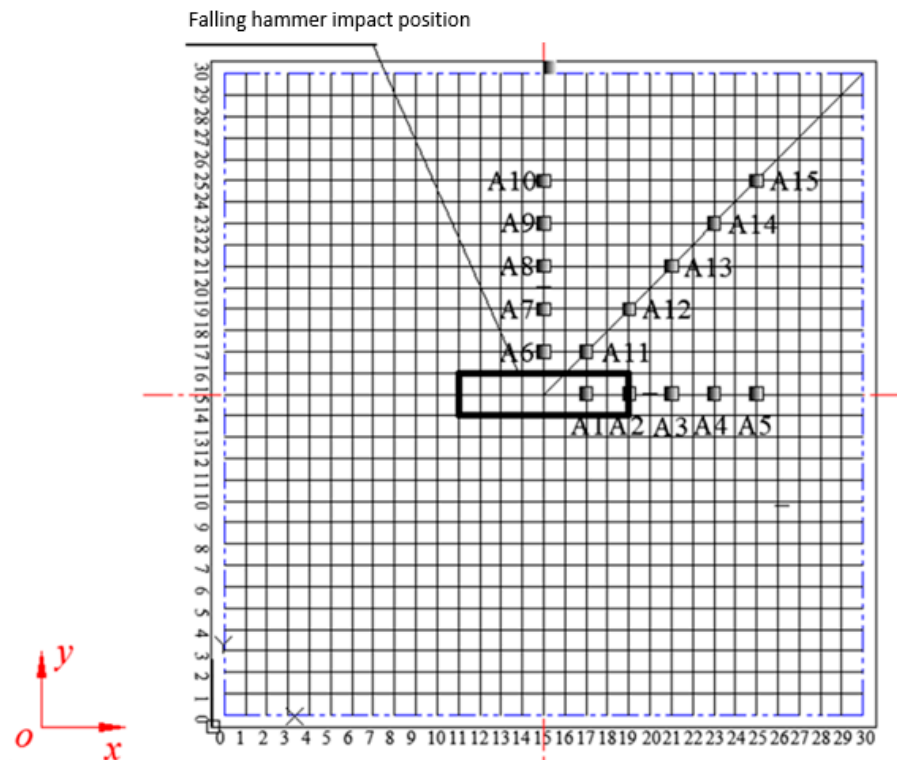


Figure 19. The positions of measuring points (unit: mm).

3.4.2. Force–Time Curve of Collision

The impact force–time curve obtained from the simulation using the MMC failure criterion is illustrated in Figure 20. It is evident that the simulated impact force–time curve aligns well with the experimental results, demonstrating a consistent overall trend. The simulation accurately predicts the early stage of the experimental curve’s impact force–time profile; however, some discrepancies are present during the middle and later stages. Concerning the peak impact force encountered during the collision, experimental measurements record a peak value of 0.547 mega-newtons (MN). In contrast, simulation-derived data present a slightly higher peak at 0.5854 MN. This indicates a deviation of 7.02% from the experimentally determined figure. Notwithstanding this difference, the margin of error falls within an acceptable range for such simulations in marine collision analysis [23,25], substantiating the simulation’s overall validity and precision. However, it was observed that the simulated impact duration exceeded the experimental impact time, which may be attributed to the fact that the boundary conditions of the specimen in the experiment are not ideally rigidly fixed.

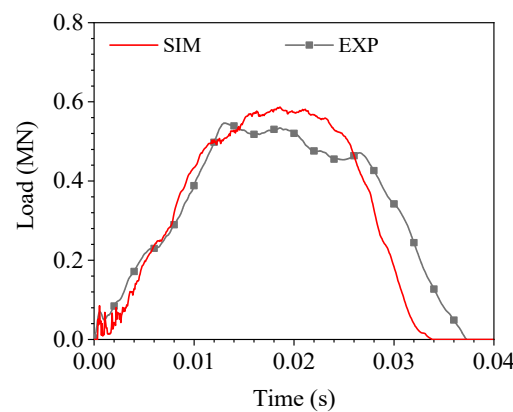


Figure 20. The force–time curve calculated by revised MMC failure criterion.

4. Discussion

The foregoing discussion detailed the calibration of the MMC metal failure criterion, which demonstrated favorable outcomes when applied to material experiments as well as drop-weight impact test simulations. Building upon this, simulation studies were conducted on plate frame structure collision scenarios under various failure criteria and mesh sizes to further ascertain the robustness of the MMC failure criterion.

4.1. Common Fracture Failure Criteria in Ship Collision Simulation

Over the past few decades, with the widespread application of the finite element method (FEM) in the field of ship collisions, the failure criteria used in ship collision simulations have become a hot topic of interest among researchers internationally and have seen significant developments. To further verify the accuracy of the MMC failure criterion, two commonly applied criteria in ship collision simulations were selected for comparative analysis: the equivalent plastic strain (EPS) criterion and the RTCL failure criterion.

4.1.1. Equivalent Plastic Strain Criterion

The critical equivalent plastic strain criterion, also known as the constant plastic strain criterion, defines that material undergoes localized fracturing when the value of the equivalent plastic strain reaches a critical level, as shown in Equation (18):

$$\bar{\epsilon} = \frac{\sqrt{2}}{3} \sqrt{(\epsilon_1 - \epsilon_2)^2 + (\epsilon_2 - \epsilon_3)^2 + (\epsilon_3 - \epsilon_1)^2} = \bar{\epsilon}_f \tag{18}$$

In the formula, $\bar{\epsilon}$ represents the equivalent plastic strain, while $\epsilon_1, \epsilon_2, \epsilon_3$ signify the first, second, and third principal strains, respectively. $\bar{\epsilon}_f$ denotes the critical equivalent plastic strain. This critical value is often referred to as the maximum plastic strain or critical strain, and it is typically determined through uniaxial tensile tests. However, this failure criterion overlooks the influence of stress states on material failure. For instance, it assumes that materials can fracture under pure compression, which contradicts empirical experimental phenomena. Since the failure strain of this criterion is derived from uniaxial tensile testing, it is sensitive to mesh size. Therefore, when simulating with this failure criterion, it is important to scale the failure strain according to the actual mesh size used.

4.1.2. RTCL Failure Criterion

Rice and Tracey [26], building upon the foundation of micromechanics of damage, have derived an expression for the Rice–Tracey ductile failure criterion by studying the growth behavior of internal defects in materials (such as spherical voids) under loading. The expression for the Rice–Tracey criterion is presented in Equation (19). This criterion is capable of accurately predicting the growth of voids and is applicable over a wide range of triaxialities.

$$D = \int_0^{\bar{\epsilon}_f} \exp(1.5\eta) d\bar{\epsilon} \tag{19}$$

Subsequently, Cockcroft and Latham [27] proposed a failure criterion based on the equivalent plastic strain corrected for the maximum principal stress, as shown in Equation (20). The Cockcroft–Latham criterion exhibits good predictive capabilities for ductile shear failure within a low range of stress triaxiality.

$$D = \int_0^{\bar{\epsilon}_f} \sigma_1 d\bar{\epsilon} \tag{20}$$

Tornqvist [5], by integrating the Rice–Tracey and Cockcroft–Latham criteria along with a cutoff value where fracture failure does not occur, introduced the RTCL criterion suitable for a broader range of stress states, as presented in Equations (21) and (22):

$$D = \frac{1}{\bar{\epsilon}_f} \int_0^{\bar{\epsilon}_f} \begin{cases} 0 & \eta < -\frac{1}{3} \\ \frac{\sigma_1}{\bar{\sigma}} d\bar{\epsilon}^P & -\frac{1}{3} \leq \eta \leq \frac{1}{3} \\ \exp\left(\frac{3\eta-1}{2}\right) d\bar{\epsilon}^P & \eta > \frac{1}{3} \end{cases} \tag{21}$$

$$\frac{\sigma_1}{\bar{\sigma}} = \frac{2 + 2\eta\sqrt{12 - 27\eta^2}}{3\eta + \sqrt{12 - 27\eta^2}} \tag{22}$$

In the formula, D represents the damage factor, which leads to the elimination of the element when D = 1 reaches a critical value. $\bar{\epsilon}^p$ denotes the equivalent plastic strain, η is the stress triaxiality, and $\bar{\epsilon}_f$ signifies the fracture strain that also serves as the sole input parameter for the RTCL failure criterion. This parameter can be determined through uniaxial tensile testing. The RTCL criterion is relatively sensitive to mesh size. Therefore, it is essential to scale the failure strain obtained under uniaxial tensile conditions to reduce its mesh size sensitivity. The fracture scaling law is expressed as shown in Equation (23):

$$\epsilon_f = \epsilon_r + (\epsilon_n - \epsilon_r) \frac{t_e}{l_e} \tag{23}$$

Within this context, ϵ_r corresponds to the strain at which material diffuse necking occurs, and ϵ_n is the fracture strain under uniaxial tensile conditions when $t_e/l_e = 1$. Here, t_e represents the element thickness, and l_e denotes the element size. By combining Equations (22) and (23), one can derive the RTCL failure criterion, which is related to mesh size and stress triaxiality.

4.2. Comparative Analysis of Impact Responses of Stiffened Panels under Drop-Weight Collisions Using Different Failure Criteria

The stress damage contour plots obtained using the two failure criteria were compared with the damage photos from the plate frame test, as shown in Figures 21 and 22. It is observable that the stress levels and distributions calculated by the three failure criteria are relatively consistent. Among these, the failure criteria that take into account the state of stress, such as RTCL and MMC, are capable of accurately predicting the “crescent-shaped” rupture in the plate frame panels. In contrast, the EPS failure criterion, due to its lack of consideration for the relationship between the failure strain of elements and the state of stress, can only predict the shear rupture at the initial contact between the wedge-shaped hammer head and the panel. It is completely unable to foresee the damage propagation at both ends of the initial rupture.

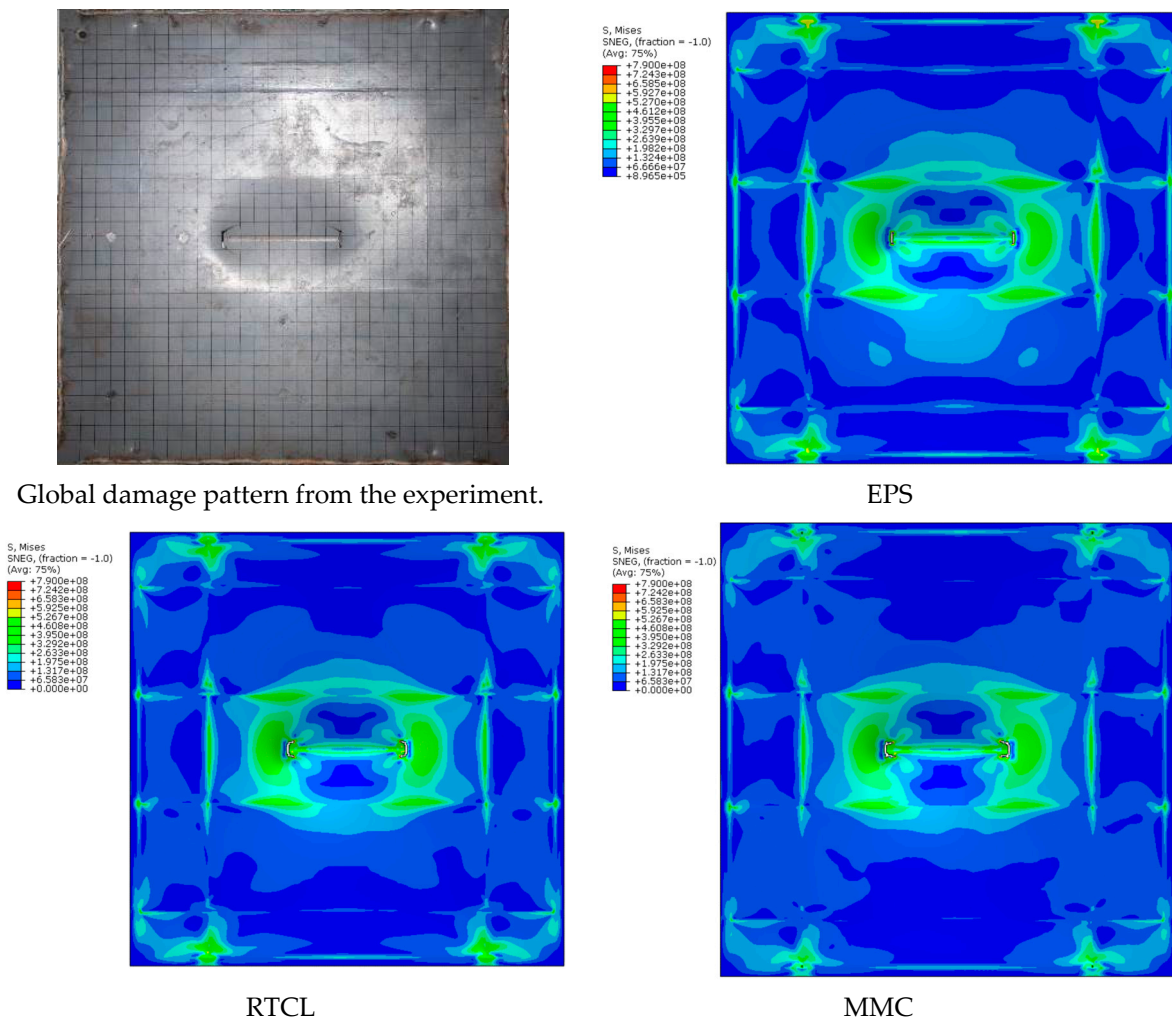


Figure 21. Damage prediction of different failure criteria for drop hammer collision conditions (overall).

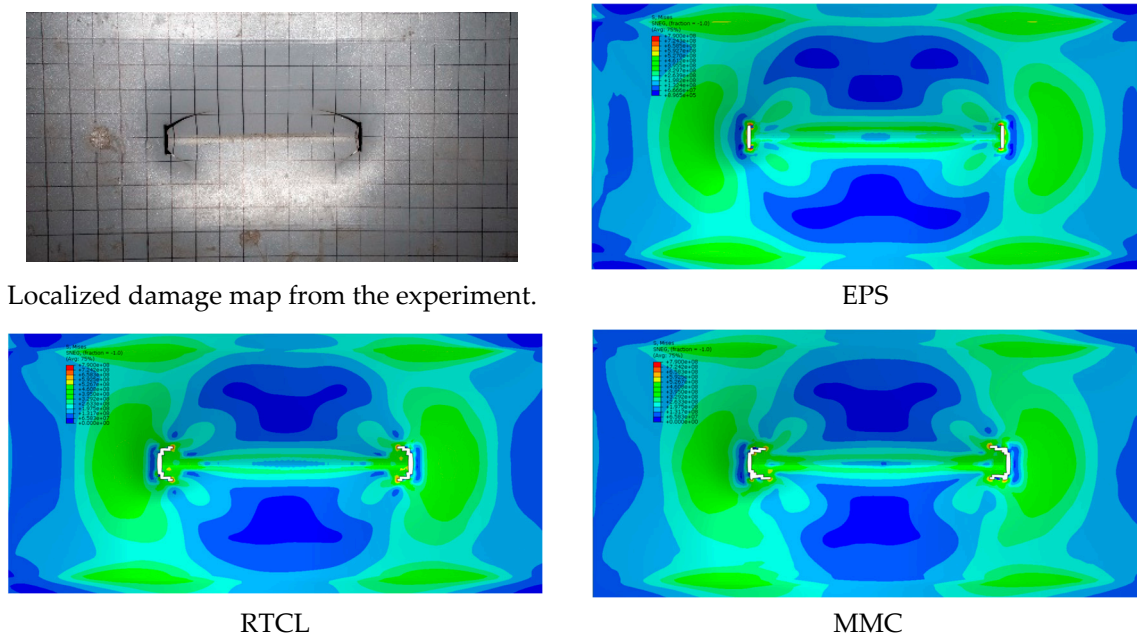


Figure 22. Damage prediction of different failure criteria for drop hammer collision conditions (local).

The simulation results for the EPS, RTCL, and MMC failure criterion were compared with experimental data, as shown in Figure 23. Since all other settings are consistent across the simulations except for the failure criteria, it is observed that the three simulation curves for each data set coincide completely during the initial phase of the collision. It is only when element failure occurs that the EPS and RTCL curves begin to diverge from the MMC curve. The peak collision force and the termination time of the collision force indicates that the MMC failure criterion provides a closer prediction of the collision force–time curve compared to the experimental results. This demonstrates the effectiveness of the MMC failure criterion.

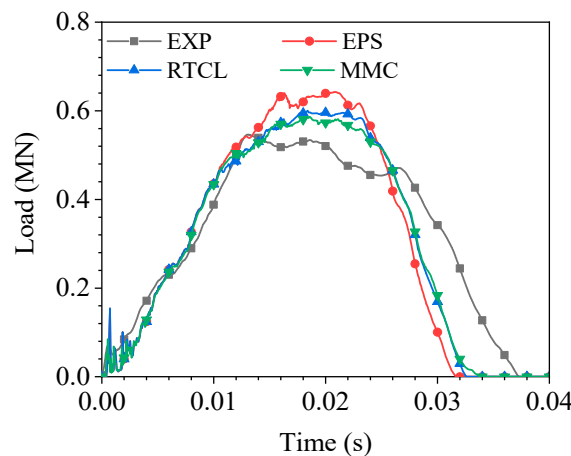


Figure 23. The force–time curve calculated by different failure criteria.

A comparative analysis of collision force peaks obtained from simulations using EPS, RTCL, and the modified MMC failure criterion against experimental peak values is presented in Table 7. It can be observed that the peak collision force error for the MMC failure criterion is 7.02%; for the RTCL failure criterion, it is 9.76%; and, for the EPS failure criterion, it is 17.48%. A comparative analysis of collision energy obtained from simulations using EPS, RTCL, and the modified MMC failure criterion against experimental collision energy values is presented in Table 8. It can be observed that the collision energy error for

the MMC failure criterion is 0.02%; for the RTCL failure criterion, it is 0.20%; and, for the EPS failure criterion, it is 2.11%. The simulation results utilizing the MMC failure criterion demonstrate smaller errors compared to those using the EPS and the RTCL failure criteria, further substantiating the effectiveness and superiority of the MMC failure criterion.

Table 7. Comparison of simulation collision force peak with experimental data.

Failure Criterion	Collision Force Peak (MN)	Error (%)
EXP	0.547	0
MMC	0.5854	7.02
RTCL	0.6004	9.76
EPS	0.6426	17.48

Table 8. Comparison of simulation collision energy with experimental data.

Failure Criterion	Collision Energy (KJ)	Error (%)
EXP	22.51	0
MMC	22.51	0.02
RTCL	22.46	0.20
EPS	22.03	2.11

4.3. Mesh Size Sensitivity Study of the MMC Failure Criterion

To validate the accuracy of the mesh sensitivity correction for the MMC failure criterion, a mesh size sensitivity analysis was conducted for the simulation of stiffened plate collisions. Given that the purpose of this work is to examine a small breach in the event of a minor ship accident and that a bigger mesh size is not suitable for accurately characterizing a smaller breach, the original geometric model was discretized into meshes of 4 mm, 6 mm, and 8 mm sizes, and finite element calculations were performed using the MMC failure criterion with corrected mesh sensitivity. The results of the mesh discretization are shown in Figure 24.

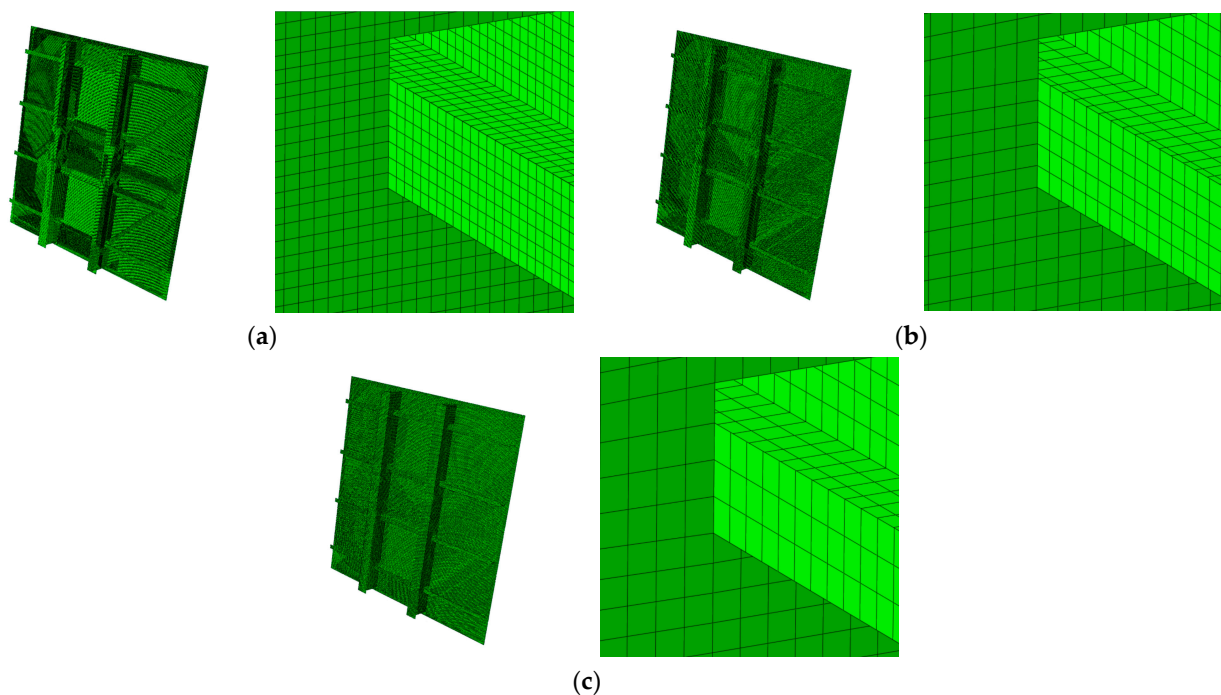


Figure 24. Finite element models of stiffened panels with different mesh sizes. (a) Mesh feature length of 4 mm; (b) mesh feature length of 6 mm; (c) mesh feature length of 8 mm.

The simulated results of the panel frame collision under different mesh sizes are depicted in Figures 25 and 26. It is observable that the overall deformation patterns of the panel frame are essentially consistent across the three mesh sizes, with the central impact area exhibiting a downward dent, and the large deformation zones of the panel being constrained by the stiffeners. The distribution of stress is largely uniform, with high-stress regions concentrated around the hammer impact tearing location. The morphology of the panel breaches is broadly similar, with each mesh size capable of replicating the initial shear breaches at both ends caused by the wedge-shaped hammer head. However, due to the influence of mesh size, although the 6 mm and 8 mm meshes can also simulate the subsequent tearing breaches, the experimentally observed breaches exhibit a “crescent” shape with elongated ends, which the coarser mesh sizes fail to accurately represent regarding the directional propagation of the tears. Therefore, employing a 4 mm mesh size can more accurately simulate the deformation and damage of the panel frame under the hammer impact conditions.

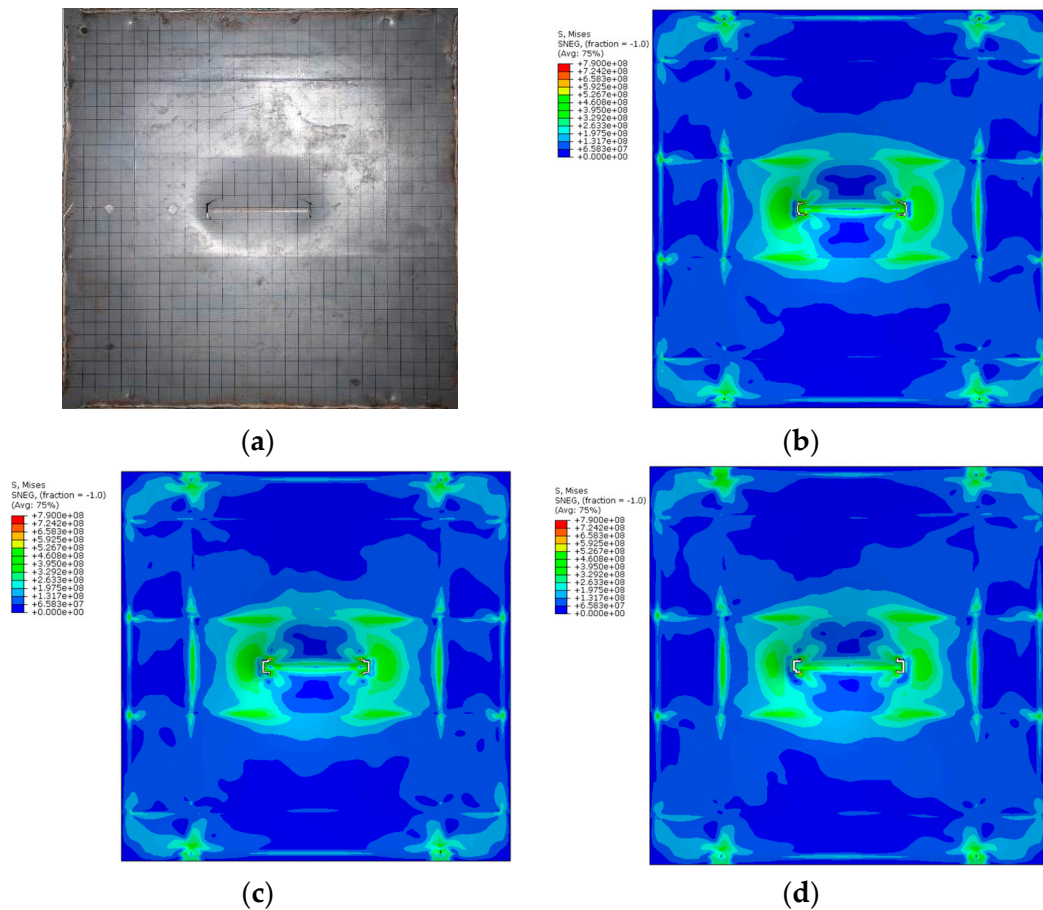


Figure 25. The overall contour of von Mises stress of different mesh size models under drop hammer collision conditions. (a) Test damage diagram; (b) 4 mm finite element model; (c) 6 mm finite element model; (d) 8 mm finite element model.

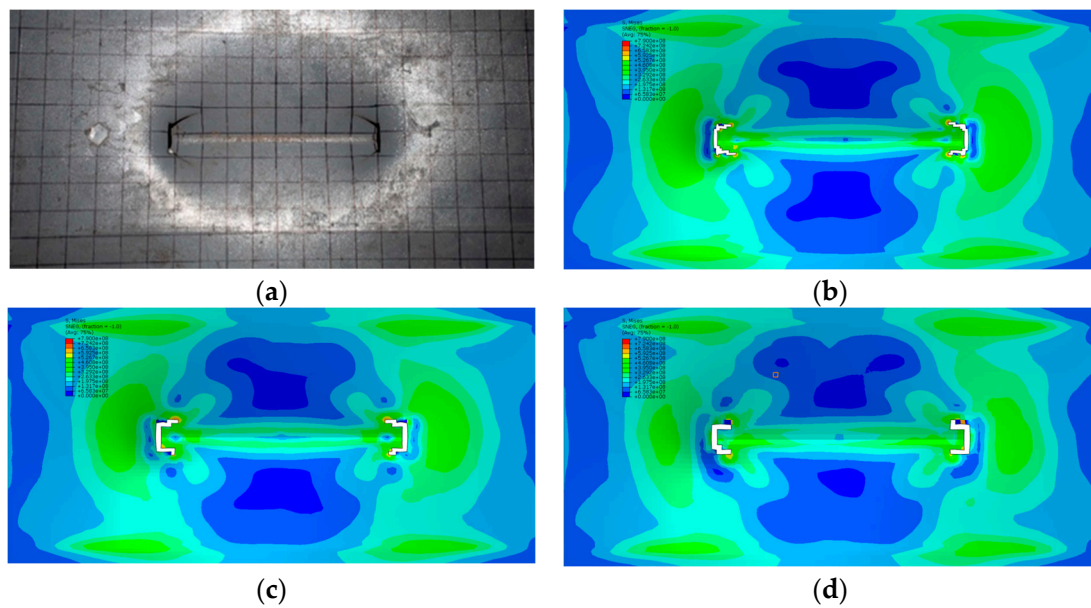


Figure 26. Local contour of von Mises stress of different mesh size models under drop hammer collision condition. (a) Test damage diagram; (b) 4 mm finite element model; (c) 6 mm finite element model; (d) 8 mm finite element model.

A comparison of the collision force curves under different mesh sizes with experimental results is shown in Figure 27. It can be observed that, in the early stage of the curves, before any damage to the panel frame occurs, the collision force–time curves for different mesh sizes are in good agreement. After the onset of damage, the three curves exhibit some differences, but, overall, they are closely aligned. It can be concluded that the finite element results for various mesh sizes are convergent. This outcome substantiates the effectiveness of the mesh size sensitivity correction applied to the MMC failure criterion.

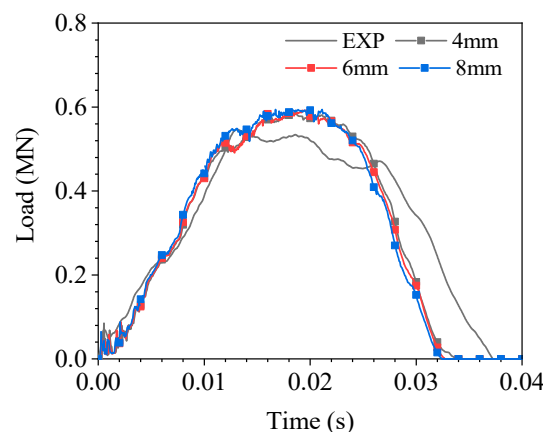


Figure 27. The force–time curve corresponding to different mesh models.

5. Conclusions

This study uses simulations and tests to calibrate and apply the MMC failure criterion to the crashworthiness of hull plate structures. The ship collision simulation’s issue with the input of metal materials has been resolved, where a typical plate frame structure is selected for collision analysis based on the collision mode of minor collisions of ships, calibrating the MMC failure criterion for marine high-strength steel and furthering this by implementing a mesh sensitivity correction that considers the stress state. Through panel frame drop hammer impact experiments and tensile test simulations, the superiority of the modified MMC failure criterion was confirmed. This establishes a theoretical foundation

for the safety design and assessment of hull beam structures going forward. The main conclusions are as follows:

(1) Utilizing MATLAB optimization tools, the three-dimensional fracture surface and two-dimensional fracture trajectory of the MMC failure criterion were fitted, and a mesh size sensitivity correction considering the influence of stress states was conducted. By including the MMC failure criterion into the Abaqus VUMAT subroutine and contrasting the outcomes of the simulation and experiment, the validity of the modified MMC failure criterion was confirmed.

(2) Simulations using the MMC failure criterion were carried out for the drop hammer collision test on the stiffened plate of ship structures, where the damage response mode under impact from a wedge-shaped head was studied, and the deformation mechanism was analyzed. A comparison between experimental and simulated damage deformation states and collision force–time curves verified the reliability of the MMC failure criterion.

(3) Simulations of the panel frame structure of a ship subjected to drop hammer collision were conducted using different failure criteria. The damage deformation contour plots and collision force curves were compared, indicating that the stress-state-aware failure criterion could more accurately simulate the deformation pattern of the breaches. Taking into account both the breach and the collision force–time curves, the MMC failure criterion showed a closer agreement with experimental results compared to the other two criteria.

(4) A mesh size sensitivity analysis utilizing the modified MMC failure criterion was performed. While damage states differed under various mesh sizes, the collision force–time curves were largely consistent, and the simulation results converged. This confirms the reliability of the correction method described in this paper.

(5) Under the experimental and simulation conditions, the MMC failure criterion in this study agrees well with the experiment; however, it is unclear how changing other parameters, like plate thickness and hammer shape, will impact the performance of various fracture standards. Future research may take this area of study as its direction.

The MMC failure criterion simulation and test conducted in this study serve as a guide for ship structure safety. A typical unit structure in ships is the stiffened plate, whose damage can serve as a model for actual ship damage in complicated collision scenarios and offer recommendations for the crashworthiness of ship designs. This work does not provide a comprehensive picture of the effect of the reinforced plate because it only discusses one type of plate thickness, hammer head, impact speed, impact strength, and other instances. Further tests testing various combinations of plate thickness, hammer head, impact velocity, and impact strength are necessary to have a complete understanding of the behavior of reinforcing plates.

Author Contributions: Writing—original draft, S.L.; formal analysis, S.L.; conceptualization, H.L.; writing—review and editing, K.L.; visualization, S.Z. and C.L. software, H.L.; validation, Y.L. All authors have read and agreed to the published version of the manuscript.

Funding: This research was funded by the National Natural Science Foundation of China (Grant No. 52171311; No. 52271279).

Institutional Review Board Statement: Not applicable.

Informed Consent Statement: Not applicable.

Data Availability Statement: Data are contained within the article.

Conflicts of Interest: The authors declare no conflict of interest.

References

1. Alsos, H.; Hopperstad, O.; Törnqvist, R.; Amdahl, J. Analytical and numerical analysis of sheet metal instability using a stress based criterion. *Int. J. Solids Struct.* **2008**, *45*, 2042–2055. [[CrossRef](#)]
2. Hill, R. On discontinuous plastic states, with special reference to localized necking in thin sheets. *J. Mech. Phys. Solids* **1952**, *1*, 19–30. [[CrossRef](#)]

3. Minorsky, V. *An Analysis of Ship Collisions with Reference to Protection of Nuclear Power Plants*; Sharp (George G.) Inc.: New York, NY, USA, 1958.
4. Haris, S.; Amdahl, J. Analysis of ship–ship collision damage accounting for bow and side deformation interaction. *Mar. Struct.* **2013**, *32*, 18–48. [[CrossRef](#)]
5. Törnqvist, R. *Design of Crashworthy Ship Structures*; Technical University of Denmark: Kongens Lyngby, Denmark, 2003.
6. Ehlers, S.; Broekhuijsen, J.; Alsos, H.S.; Biehl, F. Simulating the collision response of ship side structures: A failure criteria benchmark study. *Int. Shipbuild. Prog.* **2008**, *55*, 127–144. [[CrossRef](#)]
7. Storheimabe, M.; Amdahl, J.; Martens, I. On the accuracy of fracture estimation in collision analysis of ship and offshore structures. *Mar. Struct.* **2015**, *44*, 254–287. [[CrossRef](#)]
8. Driemeier, L.; Brünig, M.; Micheli, G.; Alves, M. Experiments on stress-triaxiality dependence of material behavior of aluminum alloys. *Mech. Mater.* **2010**, *42*, 207–217. [[CrossRef](#)]
9. Wang, Z.; Hu, Z.; Liu, K.; Chen, G. Application of a material model based on the Johnson-Cook and Gurson-Tvergaard-Needleman model in ship collision and grounding simulations. *Ocean Eng.* **2020**, *205*, 106768. [[CrossRef](#)]
10. Calle, M.A.G.; Alves, M. A review-analysis on material failure modeling in ship collision. *Ocean Eng.* **2015**, *106*, 20–38. [[CrossRef](#)]
11. Bai, Y.; Wierzbicki, T. Application of extended Mohr–Coulomb criterion to ductile fracture. *Int. J. Fract.* **2009**, *161*, 1–20. [[CrossRef](#)]
12. Lou, Y.; Huh, H. Evaluation of ductile fracture criteria in a general three-dimensional stress state considering the stress triaxiality and the lode parameter. *Acta Mech. Solida Sin.* **2013**, *26*, 642–658. [[CrossRef](#)]
13. Hu, Q.; Li, X.; Han, X.; Chen, J. A new shear and tension based ductile fracture criterion: Modeling and validation. *Eur. J. Mech. A/Solids* **2017**, *66*, 370–386. [[CrossRef](#)]
14. Bao, Y.; Wierzbicki, T. On fracture locus in the equivalent strain and stress triaxiality space. *Int. J. Mech. Sci.* **2004**, *46*, 81–98. [[CrossRef](#)]
15. Talebi-Ghadikolaee¹, H.; Naeni¹, H.; Mirnia, M.; Mirzai, M.; Alexandrov, S.; Gorji, H. Experimental and numerical investigation of failure during bending of AA6061 aluminum alloy sheet using the modified Mohr-Coulomb fracture criterion. *Int. J. Adv. Manuf. Technol.* **2019**, *105*, 5217–5237. [[CrossRef](#)]
16. Voormeeren, L.; Walters, C.; Tang, L.; Vredeveltdt, A. Estimation of failure parameters for finite element simulations based on a single state of stress and arbitrary stress-strain relation. In Proceedings of the ASME 2014 33rd International Conference on Ocean, Offshore and Arctic Engineering OMAE 2014, San Francisco, CA, USA, 8–13 June 2014.
17. Zhu, L.; Estefen, S.; Lourenço, M. Fracture criteria applied to numerical simulation of blowout preventer ram shearing. *Eng. Fail. Anal.* **2020**, *114*, 104596. [[CrossRef](#)]
18. Mohr, O. *Abhandlungen Aus Dem Gebiete Der Technischen Mechanik*; W. Ernst & Sohn: Berlin, Germany, 1914.
19. Bao, Y.; Wierzbicki, T. A comparative study on various ductile crack formation criteria. *J. Eng. Mater. Technol.* **2004**, *126*, 314–324. [[CrossRef](#)]
20. Yu, R.; Li, X.; Yue, Z.; Li, A.; Zhao, Z.; Wang, X.; Zhou, H.; Lu, T.J. Stress state sensitivity for plastic flow and ductile fracture of L907A low-alloy marine steel: From tension to shear. *Mater. Sci. Eng. A* **2022**, *835*, 142689. [[CrossRef](#)]
21. Dassault Systèmes. SIMULIA User Assistance 2020. Available online: https://help.3ds.com/2020/english/dssimulia_established/SIMACAESUBRefMap/simasub-c-vumat.htm?contextscope=all (accessed on 4 April 2024).
22. Ling, Y. Uniaxial true stress-strain after necking. *AMP J. Technol.* **1996**, *5*.
23. Liu, H.; Liu, K.; Wang, X.; Gao, Z.; Wang, J. On the Resistance of Cruciform Structures during Ship Collision and Grounding. *J. Mar. Sci. Eng.* **2023**, *11*, 459. [[CrossRef](#)]
24. Liu, K.; Zong, S.; Li, Y.; Wang, Z.; Hu, Z.; Wang, Z. Structural response of the U-type corrugated core sandwich panel used in ship structures under the lateral quasi-static compression load. *Mar. Struct.* **2022**, *84*, 103198. [[CrossRef](#)]
25. Liu, K.; Liu, H.; Li, Y.; Wang, Z.; Wang, J. A Simplified Method for Evaluating the Dynamic Response of the Metal Sandwich Structure under Explosion Load. *Metals* **2022**, *12*, 1933. [[CrossRef](#)]
26. Rice, J.R.; Tracey, D.M. On the ductile enlargement of voids in triaxial stress fields. *J. Mech. Phys. Solids* **1969**, *17*, 201–217. [[CrossRef](#)]
27. Cockcroft, M. Ductility and workability of metals. *J. Met.* **1968**, *96*, 2444.

Disclaimer/Publisher’s Note: The statements, opinions and data contained in all publications are solely those of the individual author(s) and contributor(s) and not of MDPI and/or the editor(s). MDPI and/or the editor(s) disclaim responsibility for any injury to people or property resulting from any ideas, methods, instructions or products referred to in the content.